ChemComm

COMMUNICATION

View Article Online
View Journal | View Issue

Cite this: *Chem. Commun.*, 2026, **62**, 3852

Received 9th December 2025,
Accepted 13th January 2026

DOI: 10.1039/d5cc07007d

rsc.li/chemcomm

Terminal-selective healing of perovskite crystals for air-fabricated high-performance flexible perovskite solar cells

Shendong Xu,[a] Yuli Tao,[b] Ke Yang,*[a] Yongtao Li,*[c] Haiying Zheng,[d] Guozhen Liu*[e] and Xu Pan*[b]

A pre-sewing strategy involving terminal-selective healing was established in order to sew structural defects and enable scalability of air-fabricated flexible perovskite solar cells. These cells show a champion power conversion efficiency (PCE) of 24.51%, and demonstrate exceptional bending stability. Corresponding minimodules with areas of 4 and 10 cm^2 also show impressive PCEs, of 22.68% and 20.53%, respectively.

Flexible perovskite solar cells (f-PSCs) combine strong light absorption, low weight, and mechanical adaptability, making them attractive for emerging applications such as wearable electronics, portable power sources, and building-integrated photovoltaics.[1–3] These advantages position f-PSCs as promising candidates for next-generation energy technologies. Despite notable progress, their performance and long-term reliability still fall behind those of rigid and tandem devices, particularly under mechanical deformation and large-area operation.[1,4,5]

A range of strategies, including crystallization control, cross-linking, and interface modification, have improved flexible perovskite film formation and solar cell efficiency.[2,5–12] However, these approaches mainly regulate bulk crystal growth or passivate shallow defects, and cannot eliminate the large number of structural defects at crystal terminals. Vacancies, dangling bonds, and local distortions inherently persist at surfaces and grain-boundary terminations. These terminal defects act as dominant centers for non-radiative recombination and as stress concentrators during bending, making defect-driven crack propagation a major bottleneck.[10–14] Although interface engineering has become central for improving carrier dynamics, current studies primarily focus on electronic passivation rather than structural reinforcement.[14] The interaction between surface modifiers and perovskite crystal terminals, and how the degree and uniformity of these reactions influence mechanical resilience, remains poorly understood.[15]

In this work, we established a terminal-selective healing strategy using F-type pseudo-halide ammonium salts on the surface of perovskite films. We reveal that the distinct reaction behaviors of different anions are governed by their ionic radii and binding affinities. In particular, the tetrafluoroborate anion (BF_4^-), whose size matches that of halide vacancies, exchanges more effectively with halide ions and anchors at deeper defect sites than other tested anions. The pre-sewing layer (PSL) that we constructed can couple strongly with undercoordinated ions, reinforcing terminal bonding while suppressing defect-assisted recombination and ionic migration. Ultimately, the treated devices achieved PCEs of 24.51%, 22.68%, and 20.53% for small-area cells and minimodules. The strengthened terminal bonding enables f-PSCs to retain over 90% of their initial efficiency after 2000 bending cycles at a 5-mm radius.

Fig. 1a shows the typical structural features of the perovskite film surface and the design conceived in this work for constructing a pre-sewing layer (PSL) through terminal-selective healing of perovskite crystals. To construct a PSL for achieving terminal-selective healing of the electronic and structural defects of the perovskite films, two ammonium salts of F-type pseudo-halide anions with halogen characteristics were used in our study. Scanning electron microscopy (SEM) imaging shows the morphologies of the control perovskite film and the perovskite films treated with hexadecyltrimethylammonium hexafluorophosphate ($HTAPF_6$) and hexadecyltrimethylammonium tetrafluoroborate ($HTABF_4$), respectively. The control film exhibits obvious grain boundaries and non-uniform grain sizes (Fig. S1b). $HTAPF_6$ treatment fills grain boundaries with continuous particulate

[a] *School of Carbon Neutrality Science and Engineering, Anhui University of Science and Technology, Hefei 231131, P. R. China. E-mail: 2023183@aust.edu.cn*
[b] *Key Laboratory of Photovoltaic and Energy Conservation Materials, Institute of Solid State Physics, Hefei Institutes of Physical Science, Chinese Academy of Sciences, Hefei 230031, P. R. China. E-mail: xpan@rntek.cas.cn*
[c] *School of Materials Science and Engineering, Anhui University of Technology, Maanshan 243002, P. R. China. E-mail: liyongtao@ahut.edu.cn*
[d] *School of Materials Science and Engineering, Dalian Jiaotong University, Dalian 116028, P. R. China*
[e] *State Key Laboratory of Fine Chemicals, School of Chemistry, Dalian University of Technology, Dalian 116024, P. R. China. E-mail: gzliu@dlut.edu.cn*

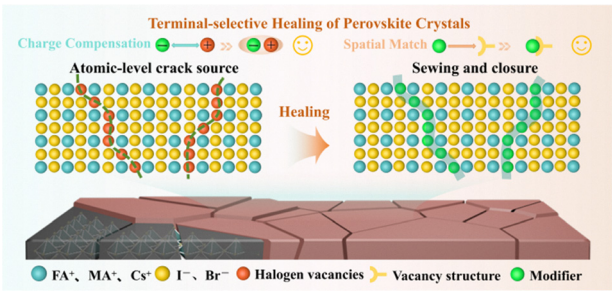

Fig. 1 Schematic diagram of the surface grain boundaries and atomic-level cracks on the crystal surface of perovskite films, and an illustration of the repair strategy.

matter (Fig. S1a), whereas $HTABF_4$ treatment forms a uniform modified layer across the entire film surface (Fig. S1c). Cross-sectional SEM analyses further corroborate variations in surface morphology induced by the different pseudo-halide anions. As shown in Fig. S2, energy-dispersive spectroscopy (EDS) characterization further reveals the characteristics of the distributions of $HTAPF_6$ and $HTABF_4$ on the respective perovskite film surfaces. We attribute this dichotomy between $HTAPF_6$ and $HTABF_4$ to the intrinsic properties of their anions (ionic radius, bonding energy), which govern surface reaction pathways and resultant morphological evolution.[16–18]

We analyzed the ionic radius differences between I^-, PF_6^- and BF_4^-. The radius of PF_6^- (255 pm) exceeds that of I^- (220 pm),[16] explaining why $HTAPF_6$ predominantly undergoes ion exchange at perovskite grain boundaries. This size mismatch prevents PF_6^- from fully occupying surface halide vacancies. Grain boundaries, with a higher defect density, further promote PF_6^- exchange/complexation. In contrast, BF_4^- (218 pm) closely matches I^- (220 pm).[17] The slightly smaller size of BF_4^- enables more effective halide vacancy compensation and direct exchange with surface halides, facilitating the formation of a uniform pre-sewing layer. Electrostatic potential diagrams of $HTABF_4$ and $HTAPF_6$ (Fig. 2a and b) reveal electron deficiency at the ammonium group and electron abundance at the pseudo-halide anions. Fluorine atoms exhibit particularly high electron density due to their strong electronegativity, endowing both salts with the capacity to passivate anion/cation defects on perovskite surfaces.[18] Crucially, BF_4^- in $HTABF_4$ displays higher negative electron density than PF_6^- in $HTAPF_6$, promoting stronger ion exchange reactions with the perovskite film. As shown in Fig. 2c and d, density functional theory calculations of energies of adsorption onto halogen vacancies show PF_6^- adsorption energy reaching 0.36 eV, significantly exceeding that of BF_4^- (0.14 eV). This higher adsorption energy for PF_6^- likely arises from stronger interactions with the lattice *via* multiple fluorine atoms. However, such strong binding anchors PF_6^- at specific defect sites (notably grain boundaries), hindering efficient ion exchange and corroborating the SEM observations. Conversely, the lower adsorption energy of BF_4^- enhances its reactivity across the perovskite surface. It efficiently compensates halogen vacancies and exchanges with surface halides *via* abundant defect sites and dangling bonds, enabling uniform PSL coverage. TOF-SIMS depth profiling confirms this mechanistic

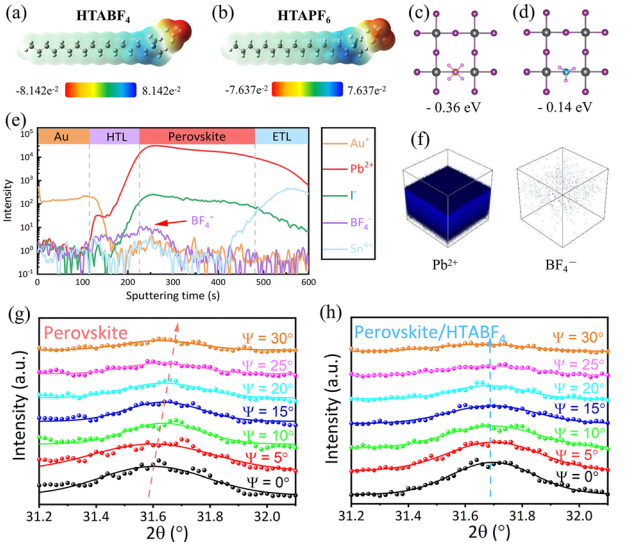

Fig. 2 Electrostatic potential density simulations of (a) $HTABF_4$ and (b) $HTAPF_6$. (c) and (d) Adsorption energies between halogen vacancies and (c) BF_4 ions or (d) PF_6 ions. (e) and (f) Tof-SIMS for 3D rendering of $HTABF_4$-treated perovskite films. (g) and (h) GIXRD patterns of (g) control and (h) $HTABF_4$-treated perovskite films at the indicated inclination angles.

difference. Devices treated with $HTABF_4$ show homogeneous BF_4^- distribution at the perovskite/HTL interface (Fig. 2e and f), while $HTAPF_6$-treated devices exhibit minimal signal intensity for PF_6^- at this interface (Fig. S3), indicating preferential accumulation of PF_6^- at grain boundaries for ion compensation/exchange.[19] Thus, BF_4^- effectively eliminates uncoordinated ions by interacting with halogen vacancies, while the ammonium cation can interconnects the surface. These actions of BF_4^- and the ammonium cation forms a pre-sewing layer that enhances both carrier transport and mechanical properties. X-ray diffraction (XRD) analysis further indicates no new species were formed during the $HTABF_4$ treatment (Fig. S4). This observation, combined with the SEM image indicate that the surfaces of the films treated with BF_4^- anion salts are more prone to ion exchange or compensation reactions, subsequently leading to surface reorganization (formation of a pre-sewing layer).

Grazing incidence X-ray diffraction (GIXRD) was employed to analyze film stress–strain relationships. As shown in Fig. 2g and h, increasing the film inclination angle (Ψ) from 0 to 30° shifts the diffraction peaks toward higher angles for untreated perovskite films, whereas the peaks in $HTABF_4$-treated films remain stable. This result confirms that untreated films exhibit lattice expansion strain at their surfaces, and that $HTABF_4$ treatment mitigates uneven expansion *via* ion exchange and repair of disordered surface atoms/defects.[9,20] Fig. S5 shows a further visualization of the functional correlation between lattice spacing d and $\sin^2(\Psi)$. X-ray photoelectron spectroscopy (XPS) measurements were taken to further characterize the binding interactions between $HTABF_4$ and perovskite components. As shown in Fig. S6, an F 1s peak is seen only in the spectra of $HTABF_4$-treated perovskite films, indicating no intrinsic fluorine content in the pristine films and confirming that all of the fluorine originates from BF_4^- ions. This result directly demonstrates

successful incorporation of BF_4^- ions—either lattice-coupled or surface-adsorbed. As shown in Fig. S7, the N 1s signal from pristine films primarily derives from organic cations (FA^+), whereas $HTABF_4$-treated films yield an additional peak from hexadecylammonium. Notably, the binding energy of the N 1s peak from the control film is seen to be shifted downward in data from the treated films, attributed primarily to N–H···F hydrogen bonding between BF_4^- ions and FA^+.[21] The element lead, a pivotal component of perovskite and governing both photoelectric properties and device stability, shows modified behavior after treatment of films with $HTABF_4$. As shown in Fig. S8, downward shifts in binding energies occur for both Pb $4f_{5/2}$ and Pb $4f_{7/2}$ peaks from the films upon their being treated with $HTABF_4$. This shift stems from strong $BF_4^-\cdots Pb^{2+}$ coordination, which weakens Pb···halogen interactions and slightly reduces the binding energy. Crucially, the metallic Pb^0 peak from the pristine film disappears post-treatment, indicating effective suppression of lead-ion reduction by $HTABF_4$.[9] Ultraviolet photoelectron spectroscopy was employed to investigate energy-level modifications in perovskite films. As shown in Fig. S9, Fermi levels are measured at 4.84 eV and 4.49 eV for the pristine and $HTABF_4$-treated films, respectively. Combining the E_{onset} values leads to values of 6.16 eV and 5.77 eV for the valence band positions of the perovskite film before and after treatment, respectively. Fig. S10 illustrates the corresponding energy-level diagram, which demonstrates that $HTABF_4$ treatment achieves optimized energy alignment, thereby enhancing interfacial transport kinetics and reducing non-radiative recombination.

Steady-state photoluminescence (PL) spectra of untreated and $HTABF_4$-treated perovskite films on non-conductive substrates (Fig. S11) show stronger PL peaks from the treated films, indicating suppressed non-radiative recombination. Fig. S12 and Table S1 present time-resolved photoluminescence (TRPL) spectroscopy results, which show the films treated with $HTABF_4$ also exhibiting longer carrier lifetime ($HTABF_4$-treated: 1126.36 ns, control: 463.96 ns). The space-charge-limited current (SCLC) method was further employed to assess the changes in film defects. The results, displayed in Fig. S13, show a defect concentration value of 3.89×10^{14} cm^{-3} for the electron-type $HTABF_4$-treated device (ITO/SnO_2/perovskite/PCBM/Au), and a value of 2.41×10^{14} cm^{-3} for the untreated device.

Fig. S14 illustrates the structure of the flexible perovskite solar cells tested. Fig. 3a presents the *J–V* curves and corresponding photovoltaic parameters of the control group devices and the devices treated with $HTABF_4$. The short-circuit current (J_{SC}), open-circuit voltage (V_{OC}), fill factor (*FF*) and photoelectric conversion efficiency (PCE) of the untreated control devices are 23.55 mA cm^{-2}, 1.15 V, 77.21%, and 20.86%, respectively. The devices treated with $HTABF_4$ show a PCE of 24.51%, and corresponding J_{SC}, V_{OC} and *FF* values of 25.11 mA cm^{-2}, 1.185 V, 82.36%, respectively (detailed parameters in Table S2). As shown in Fig. S15, forward and reverse scans for the treated devices exhibit reduced hysteresis, while the control PSC exhibits a larger hysteresis (Fig. S16, Tables S3–S4). Incident photon-to-current conversion efficiency (IPCE) analysis validates the J_{SC} improvements (Fig. S17), showing integrated currents of 24.30 mA cm^{-2} ($HTABF_4$) and

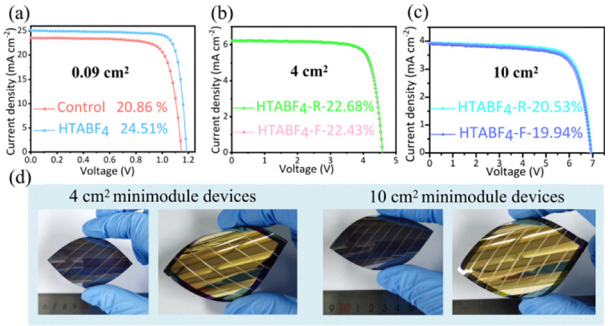

Fig. 3 (a) *J–V* curves of the best devices with untreated and $HTABF_4$-treated films. (b) and (c) *J–V* curves of the (b) 4-cm^2 and (c) 10-cm^2 modules. (d) Photographs of indicated films and devices.

22.81 mA cm^{-2} (control), consistent with the *J–V* curves. Fig. S18 shows the steady-state power output curve under AM 1.5G illumination (standard conditions) at the maximum power point. It can be observed that the devices processed by $HTABF_4$ have a steady-state output efficiency of approximately 23.8%, while the original devices have a steady-state output efficiency of approximately 19%. Subsequently, we have fabricated flexible mini modules consisting of 4 sub-cells and 6 sub-cells based on the $HTABF_4$ processing (for details of the method, see SI). Note the 4-sub-cell module exhibiting forward and reverse scan efficiencies of, respectively, 22.43% and 22.68% (Fig. 3b and Table S5)—and, delightfully, the larger 6-sub-cell module exhibiting still relatively high reverse and forward scan efficiencies of, respectively, 20.53% and 19.94% (Fig. 3c). Table S6 provides the specific photovoltaic parameters. Fig. 3d further presents photographs of the mini-module devices. Fig. S19 provides a comparison of the efficiency levels of the recently reported flexible perovskite solar cells (and Table S7 shows the detailed device structures, effective areas, preparation processes and corresponding reference information). The efficiency levels of both the small-area and mini-module devices developed in this work are at the top among devices with the same effective area.

The stability of solar cells is a crucial performance parameter that is as important as their photovoltaic characteristics. Fig. S20 presents the contact angle test results of the film before and after pre-sewing treatment. The film after pre-sewing shows a higher contact angle, indicating that it has stronger stability against water erosion. Fig. S21 illustrates the mechanism by which the pre-sewing treatment enhances the hydrophobicity of the film. Subsequently, the environmental stability levels (60 ± 5% RH) and mechanical bending ability levels (bending radius of 5 mm) of the devices were further evaluated. (Note that all of the solar cell devices are unencapsulated). Fig. S22 shows the $HTABF_4$-treated devices maintaining over 90% of their initial efficiency over the course of 2000 hours of this environmental exposure, but the efficiency of the untreated devices decreases by more than 30%. Fig. 4a presents plots of normalized f-PSC power conversion efficiency *versus* the number of bending cycles. The $HTABF_4$-treated devices exhibit superior resistance to the adverse effects of bending. Over the course of being subjected to 2000 bending cycles, the $HTABF_4$-treated devices show an efficiency attenuation of less than 10%,

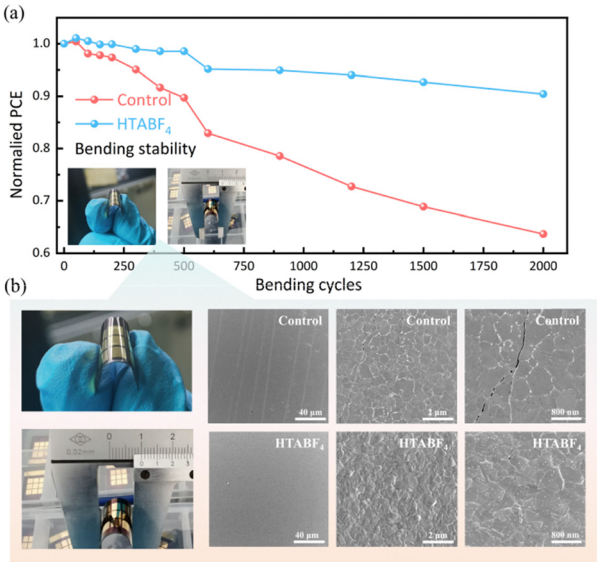

Fig. 4 (a) Plots of normalized PCE of the F-PSCs *versus* bending cycle number at a fixed bending radius of 5 mm. (b) Photographs of F-PSCs and SEM images of their films after being bent 2000 times.

while the untreated devices show an efficiency loss exceeding 30%. Microscopy images of the processed and unprocessed films subjected to 2000 bending cycles (Fig. 4b) show obvious cracks with decomposition products of suspected perovskite components near the cracks for the control film—but no obvious cracks and instead a relatively intact state for the processed target film, further verifying its strong resistance to the adverse effects of bending.

In summary, we demonstrate an effective terminal-selective healing strategy for the growth of a pre-sewing layer (PSL) at perovskite crystal terminals. This terminal-targeted regulation enables flexible $HTABF_4$-treated perovskite solar cells to deliver "champion" PCEs of 24.51% (single cells), 22.68% (4 cm^2 minimodules), and 20.53% (10 cm^2 minimodules). Critically, the PSL synergistically improves durability during bending, operational stability, and lead encapsulation: optimized devices retain >90% of the initial PCE over the entire course of 2000 bending cycles and 2000 hours of aging.

This work was financially supported by the Scientific Research Foundation for High-level Talents of Anhui University of Science and Technology (No. YJ20240014) and the National Natural Science Foundation of China (52402228), Natural Science Foundation of Liaoning Province (2025-BS-0032).

Conflicts of interest

There are no conflicts to declare.

Data availability

The data supporting this article have been included as part of the supplementary information (SI). Supplementary information: experimental details, DFT, PL/TRPL, SCLC, SEM, TOF-SIMS, XPS, device structure, contact angle measurement, and photovoltaic performance results. See DOI: https://doi.org/10.1039/d5cc07007d.

References

1 L. A. Castriotta, M. A. Uddin, H. Jiao and J. Huang, *Adv. Mater.*, 2025, **37**, 2408036.
2 J. Liu, D. Zheng, K. Wang, Z. Li, S. Liu, L. Peng and D. Yang, *Joule*, 2024, **8**, 944–969.
3 C. Jiang, T. Qin, L. Tan, H. Li, J. Zhou, M. Li, Z. M. Dang, L. Ding, Q. Xiong and C. Yi, *Adv. Energy Mater.*, 2024, **14**, 2304093.
4 S. Liu, J. Li, W. Xiao, R. Chen, Z. Sun, Y. Zhang, X. Lei, S. Hu, M. Kober-Czerny, J. Wang, F. Ren, Q. Zhou, H. Raza, Y. Gao, Y. Ji, S. Li, H. Li, L. Qiu, W. Huang, Y. Zhao, B. Xu, Z. Liu, H. J. Snaith, N.-G. Park and W. Chen, *Nature*, 2024, **632**, 536–542.
5 Z. Xu, R. Yu, T. Xue, Q. Guo, Q. Lv, C. Zhang, E. Zhou and Z. Tan, *Energy Environ. Sci.*, 2025, **18**, 4324.
6 W. Jiang, G. Qu, X. Huang, X. Chen, L. Chi, T. Wang, C.-T. Wong, F. R. Lin, C. Yang, Q. Jiang, S. Wu, J. Zhang and A. K.-Y. Jen, *Nature*, 2025, **646**, 95–101.
7 P. Liu, H. Wang, T. Niu, L. Yin, Y. Du, L. Lang, Z. Zhang, Y. Tu, X. Liu, X. Chen, S. Wang, N. Wu, R. Qin, L. Wang, S. Yang, C. Zhang, X. Pan, S. (Frank) Liu and K. Zhao, *Energy Environ. Sci.*, 2024, **17**, 7069–7080.
8 W. Zhang, J. Liu, W. Song, J. Shan, H. Guan, J. Zhou, Y. Meng, X. Tong, J. Zhu, M. Yang and Z. Ge, *Sci. Adv.*, 2025, **11**, eadr2290.
9 Z. Li, C. Jia, H. Wu, Y. Tang, J. Zhao, Z. Su, X. Gao, S. Qiu, H. Yuan and M. Li, *Angew. Chem., Int. Ed.*, 2025, **64**, e202421063.
10 X. Sun, W. Shi, T. Liu, J. Cheng, X. Wang, P. Xu, W. Zhang, X. Zhao and W. Guo, *Science*, 2025, **388**, 957–963.
11 Q. Zhao, *Nat. Energy*, 2024, **9**, 920–921.
12 X. Zhu, Y. Li, Q.-Z. Li, N. Wang, S. Yang, X. Gao, L. Zhang, P. Wang, Z. Liang, J. Li, K. Wang, S. (Frank) Liu and D. Yang, *Adv. Mater.*, 2025, **37**, 2419329.
13 Z. Li, C. Jia, Z. Wan, J. Cao, J. Shi, J. Xue, X. Liu, H. Wu, C. Xiao, C. Li, M. Li, C. Zhang and Z. Li, *Nat. Commun.*, 2025, **16**, 1771.
14 H. Li, C. Liu, Y. Guo, H. Wu, X. Zhang, H. Tan, Z. Zhang, G. Zhou, X. Qiu, H. Wen, T. Yin and S. Huang, *Adv. Funct. Mater.*, 2025, e14162.
15 R. Wang, J. Zhang, Y. Cao, N. Yan, Y. Li, H. Zhang, D. Qi, J. Pi, L. Zhang, X. Gao, Y. Liu, S. (Frank) Liu and J. Feng, *Adv. Funct. Mater.*, 2025, e17633.
16 J. Tao, X. Liu, J. Shen, S. Han, L. Guan, G. Fu, D.-B. Kuang and S. Yang, *ACS Nano*, 2022, **16**, 10798–10810.
17 J. Zhang, S. Wu, T. Liu, Z. Zhu and A. K.-Y. Jen, *Adv. Funct. Mater.*, 2019, 1808833.
18 J. Wang, H. Ma, A. Wang, Z. Li, J. Dong, Y. Liu, S. Gao, S. Yan, X. Chen,Y. Li, Z. Wu, W. Xu, F. Liu, F. Wang, W. Huang and T. Qin, *Matter*, 2022, **5**, 2209–2224.
19 J. Chen, S.-G. Kim and N.-G. Park, *Adv. Mater.*, 2018, **30**, 1801948.
20 Z. Lv, Z. Wang, G. Liu, Y. Gao, S. Li, Z. Liu, M. Xu, J. Cheng, W. Zhao, W. Lu, P. Wang, J. Wei, M. Wang, W. Tian, W. Li, Y. Yan, J. Bian and Y. Shi, *Adv. Mater.*, 2025, e13600.
21 N. Li, S. Tao, Y. Chen, X. Niu, C. K. Onwudinanti, C. Hu, Z. Qiu, Z. Xu, G. Zheng, L. Wang, Yu Zhang, L. Li, H. Liu, Y. Lun, J. Hong, X. Wang, Y. Liu, H. Xie, Y. Gao, Y. Bai, S. Yang, G. Brocks, Qi Chen and H. Zhou, *Nat. Energy*, 2019, **4**, 408–415.